AFRL-AFOSR-UK-TR-2021-0022

Nonlinear and correlated dynamics of the interaction of intense ultra-short optical pulses with materials: application to plasmonics, nanostructuring, high harmonic, and THz generation

Apostolova, TZVETA
NEW BULGARIAN UNIVERSITY
21
MONTEVIDEO STR.
SOFIA, STOLICHNA, 1618
BGR

08/02/2021
Final Technical Report

Air Force Research Laboratory
Air Force Office of Scientific Research
European Office of Aerospace Research and Development
Unit 4515 Box 14, APO AE 09421

REPORT DOCUMENTATION PAGE

Form Approved
OMB No. 0704-0188

1. REPORT DATE *(DD-MM-YYYY)*	**2. REPORT TYPE**	**3. DATES COVERED** *(From - To)*
02-08-2021	Final	15 Dec 2018 - 14 Dec 2020

4. TITLE AND SUBTITLE
Nonlinear and correlated dynamics of the interaction of intense ultra-short optical pulses with materials: application to plasmonics, nanostructuring, high harmonic, and THz generation

5a. CONTRACT NUMBER

5b. GRANT NUMBER
FA9550-19-1-7003

5c. PROGRAM ELEMENT NUMBER
61102F

6. AUTHOR(S)
TZVETA Apostolova

5d. PROJECT NUMBER

5e. TASK NUMBER

5f. WORK UNIT NUMBER

7. PERFORMING ORGANIZATION NAME(S) AND ADDRESS(ES)
NEW BULGARIAN UNIVERSITY
21
MONTEVIDEO STR.
SOFIA, STOLICHNA 1618
BGR

8. PERFORMING ORGANIZATION REPORT NUMBER

9. SPONSORING/MONITORING AGENCY NAME(S) AND ADDRESS(ES)
EOARD
UNIT 4515
APO AE 09421-4515

10. SPONSOR/MONITOR'S ACRONYM(S)
AFRL/AFOSR IOE

11. SPONSOR/MONITOR'S REPORT NUMBER(S)
AFRL-AFOSR-UK-TR-2021-0022

12. DISTRIBUTION/AVAILABILITY STATEMENT
A Distribution Unlimited: PB Public Release

13. SUPPLEMENTARY NOTES

14. ABSTRACT
Developed Quantum Monte-Carlo computer model combined with system of vector nonlinear envelope equations and time dependent Schrodinger Equation and verified against multiple known ultra intense laser interactions with matter. The simulation developed simultaneously describes changes in the material properties and the polarization dynamics of the laser pulse by combining the developed theoretical tools for numerical solution of the time-dependent Schrödinger equation and the system of vector nonlinear envelope equations (VNEE). Photoionization, non-linear polarization and high-harmonic generation (HHG) in semiconductor and dielectric materials will be modeled by solving numerically the time-dependent Schrodinger equation (TDSE) with empirical ionic pseudopotentials to represent the static electronic band structure. Also, Simulated Optical Parametric Oscillator (OPO) single and triple harmonic generation and frequency conversion using an ab initio approach.

15. SUBJECT TERMS

16. SECURITY CLASSIFICATION OF:			**17. LIMITATION OF ABSTRACT**	**18. NUMBER OF PAGES**	**19a. NAME OF RESPONSIBLE PERSON**
a. REPORT	**b. ABSTRACT**	**c. THIS PAGE**			NATHANIEL LOCKWOOD
U	U	U	SAR	21	**19b. TELEPHONE NUMBER** *(Include area code)* 314-235-6005

FINAL SCIENTIFIC PERFORMANCE REPORT

Grant FA9550-19-1-7003

"Nonlinear and correlated dynamics of the interaction of intense ultra-short optical pulses with materials”

Principal Investigator
Assoc. Prof. Tzveta Apostolova,
Institute for Advanced Physical Studies, New Bulgarian University and
Institute for Nuclear Research and Nuclear Energy, Bulgarian Academy of Sciences

Participants
Prof. Ivan P. Christov, Physics Department, Sofia University
Prof. Lubomir Kovachev, Institute of Electronics, Bulgarian Academy of Sciences

Period of Performance March 2019 to July 2021

Broad-band femtosecond pulses, λ^3 diffraction and managing of electron mirrors

Attosecond and femtosecond laser pulses with few cycles under envelope are of interest for studies of atomic and molecular dynamics and generation of high intensity optical fields. Investigating the diffraction of attosecond pulses the authors (Phys. Rev. Lett. 92 (6) (2004) 063902) observed that after interaction with solid targets electron bunches with same duration and shape as that of the intensity profile of the laser pulses are created. The experimental and theoretical investigations of such pulses describe one unexpected diffraction, connected with parabolic deformation of their intensity profile at few diffraction lengths. This deformation was called λ3 diffraction and is of great interest for possibility to build electron mirrors for high intensity laser facilities in addition to techniques, developed in the standard electron optics. In our previous investigations in (J. Opt. Soc. Am. A 25 (9) (2008) 2232–2243, J. Opt. Soc. Am. A 25 (12) (2008) 3097–3098 and in J. Phys.: Conf. Ser. 594 (2015) 012023) it was shown that this phenomenon can be described analytically by solving linear non-paraxial evolution amplitude equation of the electrical field. It was demonstrated that broad-band femtosecond pulses ($\Delta kz \approx k0$) diffract also in λ3 regime. As a result, it is shown that Fresnel's law does not work for broad-band laser pulses and their diffraction is similar to attosecond ones. By using diffraction grating or other optical dispersion elements the spectrum of the femtosecond pulses can be extended and the sign of the chirp parameter can be changed. In the presented work, it is studied numerically more precisely the influence of the sign and value of the chirp parameter on the linear evolution of phase modulated femtosecond pulses.

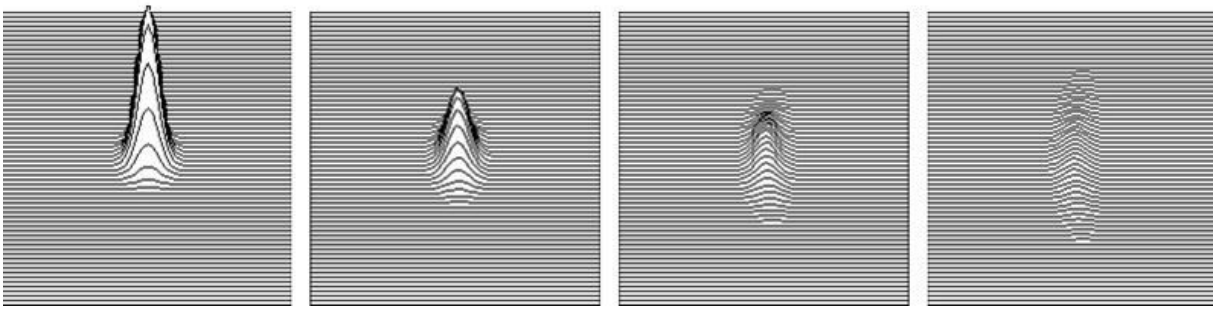

z=0 z=zdiff z=2zdiff z=3zdiff

Fig. 1. Side (x-z) projection of the intensity profile of 25 fs phase-modulated Gaussian pulse propagates in air at three diffraction lengths. The chirp parameter is negative a=-5 and λ3 diffraction with negative curvature of the parabolic intensity profile is observed.

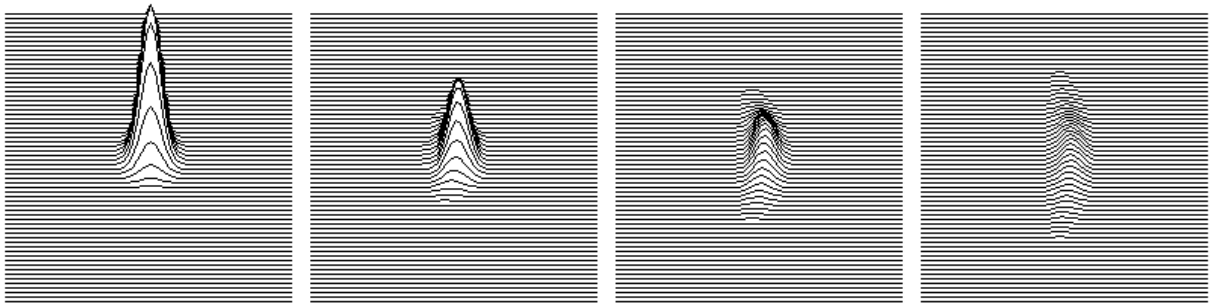

Fig. 2. Side (x-z) projection of the intensity profile of 25 fs phase-modulated Gaussian pulse propagates in air at three diffraction lengths. The chirp parameter is a=5 and λ3 diffraction with positive curvature of the parabolic intensity profile is observed.

For negative chirp the diffraction is also of λ3 type, but with the parabolic deformation of the intensity profile inverted with respect to the axis of propagation Oz. Thus, by properly used chirp parameters this process can be managed and it is possible to obtain parabolic intensity profiles with different curvature and sign. The described phenomenon allows to be created converging and diverging electron mirrors with different focal lengths. The creation and manipulating of such mirrors is of great interest for high intensity lasers, where the usual optical elements cannot be used due to optical damages. The basic problem is to create initially intensity profiles of laser pulses with different parabolic profiles. In our previous works cited above, it was shown that this phenomenon can be solved in the frame of linear non-paraxial evolution equation of the amplitude of the electrical field. Solving numerically this equation for phase modulated femtosecond pulses (20–30 fs) we demonstrated that broad-band pulses diffract in λ (3) regime. By changing the sign and the value of the chirp parameter we obtain parabolic intensity profiles with different curvature and sign with respect to the axis Oz. By properly used chirp parameters of the fs pulses the process of creation of electron bundles with arbitrary forms can be managed. Thus, different kinds of converging or diverging electronic mirrors can be created.

Publication: V. Slavchev, A. Dakovaa, D. Dakova , K. Kovachev, L. Kovachev, Broad-band femtosecond pulses, λ3 diffraction and managing of electron mirrors, Optik, V 202, pp 162311 (2020), ISSN 0030-4026,https://doi.org/10.1016/j.ijleo.2019.01.101.

Longitudinal optical force of laser pulses in continuous media

Up to now, the basic experimental and theoretical investigations are related to the study of radiation forces produced by laser beams and pulses acting on individual Rayleigh dielectric

particles. In this paper we explore the impact of the longitudinal force, associate with the Pointing vector and its influence on an ensemble of particles in dielectrics. Thus, the individual force applied to an atom is transformed to density force per volume. The optical response of dielectric media connected with the propagation of laser pulses is non-stationary and also is taken into account. In this paper we analyze the influence of electrical field response to longitudinal force density. In the following paper one more complete investigation on this force, including electrical and magnetic part to the Pointing vector influence on ponder-motive force is performed.
Publication: L. Kovachev, "Longitudinal optical force of laser pulses in continuous media," Proc. SPIE 11332, International Conference on Quantum, Nonlinear, and Nanophotonics 2019 (ICQNN 2019), 113320I (30 December 2019); doi:10.1117/12.2553544

Longitudinal radiation force of laser pulses and nonlinear optics of moving neutral particles

For a long time, transverse and longitudinal optical forces have been used for non-contact manipulation of small individual particles. The following question arises: What is the impact of these forces on an ensemble of a thousand particles in continuous media? The aim of this work is to find analytical expressions of the radiation force and potential densities arising from a laser pulse propagating in dielectric media. This allows us to find an effective averaged longitudinal real force at the level of the laser pulse spot. The force obtained is proportional to the initial pulse energy and inversely proportional to its time duration. In the femtosecond region, the force becomes strong enough to confine neutral particles into the pulse envelope and translate them with the group velocity in gases. In solids, as silica for example, the longitudinal force of a femtosecond pulse is significantly greater than the molecular forces. Thus, the fine ablation in silica with short pulses may be due to this longitudinal force, which breaks down the molecular bonds. We investigate longitudinal radiation force in media with nonstationary linear optical response.

We obtain new formula for the longitudinal part of the ponder-motor force density connected with the Pointing vector $F_z = \left(4\pi\chi^{(1)}/c\right)\partial S_z/\partial t$ or

$$F_z = -\frac{2\pi\chi^{(1)}}{cv_{gr}}\int_{-\infty}^{0}\frac{\partial^2\left|A_x(x,y,z-v_{gr}t)\right|^2}{\partial t^2}dz - \frac{2\pi\chi^{(1)}\mu}{c^2}\int_{-\infty}^{0}\frac{\partial^2\left|C_y(x,y,z-v_{gr}t)\right|^2}{\partial t^2}dz\,. \qquad (1)$$

In this equation, the longitudinal part of the force density is proportional to the second derivatives of the electrical and magnetic pulse envelopes. In cw regime, these derivatives vanish and as it is well known, Ashkin and others investigate only transvers gradient forces. In the femtosecond region, as we will see below, this force becomes significant. The difference between the atomic and optical scales gives us the chance to solve the integral of force density Eq. (1), because at a few centimetres the shape of the pulse is practically preserved. The solution of initially Gaussian

pulse in approximation of first order dispersion in the frame of spatio-temporal paraxial optics becomes:

$$F_z = -\frac{4\pi^2 \chi^{(1)} v_{gr}}{c^2 n^2} I_0 \exp\left(-\frac{x^2+y^2}{d_0^2}\right)\frac{z}{z_0^2}\left[n\exp\left(-\frac{z^2}{z_0^2}\right)+\varepsilon\exp\left(-\frac{z^2}{z_0^2}\frac{v_{ph}}{v_{gr}}\right)\right], \qquad (2)$$

where $\chi^{(1)}$ the linear susceptibility, c is is the light velocity, n is the refractive index of the media, I_0 is the peak intensity, d_0 is the pulse spot, $z_0 = v_{gr} t_0$ is the longitudinal spatial length of the pulse, $v_{ph} = c/n_0$ and v_{gr} are the phase and group velocity correspondingly. The longitudinal PM force propagates with the group velocity. The 3D image of the PM force density is plotted in Fig. 1. The pulse front attracts the ensemble of particles to the center of the pulse, and the backside pushes them again to the center.

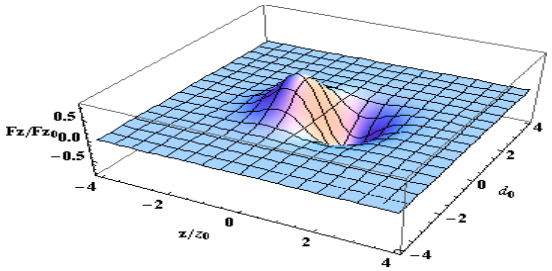

Fig. 1. Graphics of the PM longitudinal force density of a laser pulse. The pulse front attracts the ensemble of particles to the center of the pulse, and the backside pushes them again to the center.

The F_z force depends on 3D coordinates and a potential density can be introduced by $U(x,y,z) = \int_{-\infty}^{z} F_z\, dz$. The result is that the Gaussian shape of the pulse plays the role of an attractive potential. The graph of the potential density is plotted in Fig 2.

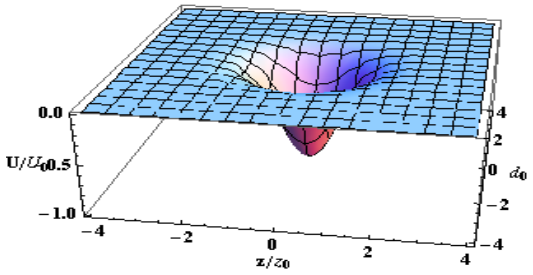

Fig. 2. Graphics of the potential density of a Gaussian laser pulse. The shape of the pulse, moving with the group velocity, plays the role of an attractive potential.

To obtain real measurable forces from the density ones, the formulae for the force density Eq. (2) and the potential density must be integrated over the whole space. As a result, after integration, we

obtain real measurable values of a real force and potential of the level of the spot of the pulse. In our examples we use t_0=100 fs laser pulse with initial energy in the range of $E_0^{laser} \cong 100nJ$. The effective potential energy is $U_z^{eff} \cong 2.7 \times 10^{-9}[J]$, which is twelve orders of magnitude greater than the Boltzmann energy of free particles in gases. The value of the longitudinal force becomes $F_{pm}^{pulse} \cong -7.02 \times 10^{-2}$ [N]. This value is six orders of magnitude greater than the molecular forces in silica. These results show that self-confinement of neutral particles into the pulse envelope is possible.

In conclusion:

1. The dipole interaction of the confinement into the pulse envelope neutral particles with the electromagnetic field will be at the carrier to envelope frequency $\omega_{CEF} = k_0 \left(v_{ph} - v_{gr} \right))$ instead the main ones ω_0. This oscillation is in the sub-THz range for gases, THz in solids, and can be measured in a direction orthogonal to the direction of the laser pulse propagation. The dipole oscillation measured in the direction of propagation will be again with carrying frequency ω_0 due to the Doppler effect.
2. In nonlinear regime the neutral moving particles will not generate at the third harmonics, but at a frequency proportional to three times carrier to envelope frequency $3\omega_{THz} = 3k_0 \left(v_{ph} - v_{gr} \right)$. Such generation was experimentally observed recently in recent papers.
3. The confined into the pulse envelope (hydrogen) *neutral* atoms admit kinetic energy of order of $E_H^{collision}$ ~1.5 GeV in a collision geometry. This energy is of order of the energy of the rest mass of one proton and high enough in a nuclear experiment.
4. The longitudinal part of the gradient term also gives longitudinal force, but as averaged ones is smaller than the term associated with the Pointing vector.

Publication: L M Kovachev, “Longitudinal radiation force of laser pulses and nonlinear optics of moving neutral particles”, Phys.: Conf. Ser. 1859 012058 (2021).

Four-photon parametric mixing in CW and pulse regimes in single mode optical fibers

The process of four photon parametric mixing can be used to convert the input laser sources, working in CW and pulse regimes, into light at several different frequencies. An effective parametric energy conversion can be observed when phase matching conditions between the waves are satisfied. The basic theoretical investigations are focused on efficiently of the four-photon mixing and parametric gain with applications such as all-optical signal sampling, time-

demultiplexing, pulse generation and wavelength conversion. The parametric amplifiers have capacity to provide high gain and low noise at arbitrary wavelengths with proper fiber design and pump wavelength allocation. The problem with the generation of new frequencies on distances less than one coherent length in the process of parametric four-photon mixing was solved in approximation of fixed electric field of the pump wave. The idea of our research is to solve the more general problem in which it is taken into account the mutual action of the first and second order of dispersion and all real $\chi^{(3)}$ nonlinear processes on the parametric four-photon mixing. In CW regime the solutions of the problem, presented above, was solved in the form of Jacobi elliptic functions. In pulse regime we found optimal conditions, where the process of energy exchange is still effective. In this regime a quasi-periodic conversion is observed and group velocity difference between the pump and signal wave is compensated by nonlinear mechanisms.

Publication: A. Dakova, D. Dakova, Z. Andreeva, D. Georgieva, V. Slavchev, L. Kovachev, "Four-photon parametric mixing in CW and pulse regimes in single mode optical fibers," Proc. SPIE 11332, International Conference on Quantum, Nonlinear, and Nanophotonics 2019 (ICQNN 2019), 113320H (30 December 2019); doi: 10.1117/12.2553231

Energy exchange during third harmonic generation in multi-mode optical fibers

The present investigations are done for χ (3) nonlinear media, with spatial mode structure as it is the multi-mode optical fibers. In these kinds of waveguides parametrical processes can be observed under certain conditions. In standard single mode optical fibers the third-harmonic generation (THG) has typically low efficiency. This is a result of the difficulties in the realization of phase-matching conditions. There exist different techniques for reducing the wave number mismatch Δk. Thus, through the years in many experiments in multimode fibers, the effect of THG has been observed. The energy exchange is strongest when the phase matching conditions are satisfied. The main investigations are related to the problem of effective amplification of the signal - third harmonic wave. In CW regime the system of amplitude equations does not contain terms related to the group delay and dispersion. In our studies we had solved analytically the system of short-cut equations, describing the parametric processes of energy exchange between two optical waves, the main one and third harmonic in multi-mode optical fibers, including into consideration the self- and cross-phase modulation. We present a mathematical model describing the process of nonlinear interaction between two optical waves, which satisfying the phase mismatch conditions needed for the observation of THG. The second order of dispersion is neglected. We have investigated two cases – in the first we have not included the effects of self-phase modulation (SPM) and cross-phase modulation (CPM) and in the second, these effects are taken into account. The obtained solutions are in the form of Jacobi elliptic functions and describe the energy exchange between the waves.

Publication: Z Kasapeteva, A Dakova, V Slavchev, D Dakova, L Kovachev and K Kovachev, “Energy exchange during third harmonic generation in multi-mode optical fibers”, J. Phys.: Conf. Ser. 1859 012050 (2021).

Soliton regime of propagation of optical pulses in isotropic medium

The propagation of ultrashort optical pulses in nonlinear dispersive media attracts considerable attention in last few decades. The Nonlinear Schrödinger Equation (NSE) is well known and it is one of the most commonly used in the field of nonlinear optics. Pulses with picosecond and femtosecond duration are very well described by NSE, but for attosecond and phase-modulated femtosecond laser pulses, where the spectral width of the pulse is of order of the carrying frequency, the equation doesn't work. In this case, it is more convenient to use the general Nonlinear Amplitude Equation (NAE). During the propagation of ultrashort pulses in optical fibers the effects of the third order of linear dispersion and dispersion of nonlinearity become significant and they have to be taken into account. In this case it is necessary to include additional terms in the NAE, which show how the third order of linear dispersion and dispersion of nonlinearity affect the pulse propagation. In present paper we investigate analytically the influence of third order of linear dispersion and dispersion of nonlinearity on the evolution of ultrashort optical pulses and the possibility of formation of dark soliton under such conditions in medium with normal dispersion.

Publication: B. Nenova, D. Dakova, A. Dakova, V. Slavchev, L. Kovachev, “Soliton regime of propagation of optical pulses in isotropic medium under the influence of third order of linear dispersion and dispersion of nonlinearity. Dark solitons”, J. Phys.: Conf. Ser. 1859 012051 (2021).

Spatial distribution of the electric field of laser pulses in optical fibers having a gradient profile of the refractive index

In recent years, the evolution of three-dimensional optical pulses in isotropic dispersive linear and nonlinear media has been actively studied. They are used in telecommunications, in optical methods for encoding and recording information, in modern medical laser systems for precision cutting and ablation of tissues. In the present work we have investigated the dynamic of laser pulses in optical fibers with quadratic dependence of the refractive index in linear regime. The evolution of these pulses in a media with dispersion of the group velocity admits specific behavior. Gradient-index fibers are used in optical communication systems for improving their parameters. The refractive index of such kind of waveguides can be presented by the expression:

$$n = n_0(\omega) + S_g(x^2 + y^2) + n_2\left|\vec{U}\right|^2, \qquad (1)$$

where $n_0(\omega)$ and n_2 corresponds to the linear and nonlinear refractive index of the medium; $\vec{U}$ is the vector amplitude function describing the pulse’s envelope; S_g is a constant connected with the

refractive index of the fiber and $S_g(x^2+y^2)$ characterizes the spatial profile of the refractive index. Depending on the sing of the constant S_g the gradient-index waveguides can be presented in two different groups [7]:

1. $S_g < 0$ – when the constant is smaller than zero, we have *convex gradient fibers.* The linear refractive index has maximal value on the fiber axis and it decreases smoothly to the periphery of the waveguide.
2. $S_g > 0$ – when the constant is bigger than zero, then we have *concave gradient fibers*. The refractive index rises smoothly towards the periphery of the waveguide.

In our paper we search for analytical solution of the vector amplitude equation (2) in linear case ($n_2=0$), describing the propagation of laser pulses in concave gradient optical fibers ($S_g>0$).

We found new class analytical solutions which describe the evolution of components of the vector amplitude function of a laser pulse propagates in optical fibers with concave profile of the refractive index. The solutions are in the form of Bessel functions. They characterize the modal structures in the fiber. Numerical simulations of the solutions for different values of constant *n* were presented.

Publication: I Bozhikoliev, V Slavchev, A Dakova, D Dakova, K Kovachev, L Kovachev, "Spatial distribution of the electric field of laser pulses in optical fibers having a gradient profile of the refractive index. Linear case", J. Phys.: Conf. Ser. 1859 012053 (2021).

Phase-locking mechanism in non-sequential double ionization

The non-sequential double ionization is undoubtedly one of the most dramatic manifestations of electron-electron correlation in the presence of powerful laser radiation. Experiments with linearly polarized sub-100 fs pulses with intensities in the range 10^{14}-10^{16} W/cm^2 have demonstrated ionizations exceeding by order of magnitude the predictions of the standard theories where electrons are ejected independently of each other (sequential double ionization). In the case of two electrons (for example in helium) it is known that during the act of the non-sequential double ionization (NSDI) one of the electrons interacts strongly through its Coulomb potential with the other electron, which also moves under the combined action of the nuclear potential and the external field. The scattering mechanism where the accelerated electron returns back to the nucleus and knocks out the other electron, is responsible for a significant portion of the NSDI. One important indication of NSDI is the folded (knee) structure of the ionization as a function of the peak laser intensity where this ionization may remain almost constant, which is observed also in numerical simulations in reduced dimension models. While that re-collision mechanism is dominant for high intensities and long wavelengths where tunneling through the nuclear potential takes place, for lower intensity and higher frequencies the role of the re-collision is replaced by

sequential and non-sequential multiphoton ionization. The growing interest in this regime is motivated by the rapid experimental development of powerful short-wavelength sources, such as the free-electron lasers, capable of producing terawatt femtosecond VUV pulses. In the work reported here we consider NSDI in a one-dimensional helium atom for laser wavelength 248 nm. To clarify the mechanism of NSDI, we focus on the early stages of electron ionization, in which both electrons are still close to the nucleus while they "see" the growing front of the laser pulse where there is almost no tunneling. Our goal is to prove that the final ionization after the pulse is predetermined to a great extent by the early history of electron motion before the electron is ionized. Our study is favored by the fact that at the early stage of ionization the electron motion is better traceable since it does not show the chaotic nature of the quasi-free electrons in an external field. In the research we identify a new mechanism in which the early stage of electron ionization in the field of a powerful femtosecond laser pulse determines the final double ionization. Using quantum trajectories, we were able to prove that a powerful short-wavelength laser field causes injection-locking between its phase and phases of electron trajectories, which then leads to enhanced or repressed ionization in the knee range. It has been shown that both ionization and entanglement of the final electron state can easily be controlled by introducing a frequency chirp on the laser field. Our methods have allowed to determine the quantum correlations due to different ionization mechanisms.

For one dimensional model atom with soft-core Coulomb potentials, subjected to laser field $E(t)$, the Hamiltonian in atomic units reads:

$$H(x_1, x_2) = -\frac{1}{2}\frac{\partial^2}{\partial x_1^2} - \frac{1}{2}\frac{\partial^2}{\partial x_2^2} - \frac{2}{\sqrt{1+x_1^2}} - \frac{2}{\sqrt{1+x_2^2}} + \frac{1}{\sqrt{1+(x_1-x_2)^2}} - (x_1+x_2)E(t)$$

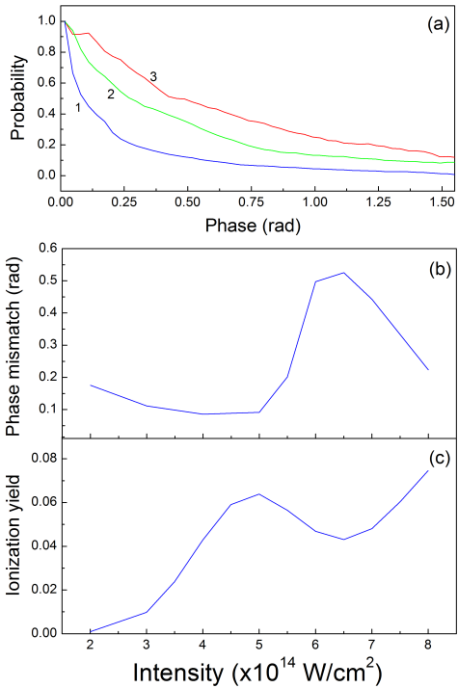

Fig. 1. (a) -Normalized smoothed histograms of the distributions of the relative phases for the two electron trajectories for different laser intensities, for the first three periods of a flat-top pulse: blue line -4.5x10^{14} W/cm^2, red line -6x10^{14} W/cm^2, green line -8x10^{14} W/cm^2; (b)-phase mismatch between the trajectories of the two electrons as function of the peak laser intensity where the knee structure is observed.

The ground state of the atom is calculated numerically by imaginary-time propagation of the time-dependent Schrodinger equation on a two-dimensional grid, which gives ground state energy of -2.238 a.u. We assume an electric field with six cycle trapezoidal envelope, with two cycle turn-on and turn-off. The key mechanism for trajectory evolution is shown in Fig.1. Clearly, if the electrons were free they would oscillate in complete phase with the laser. In order to quantify the phase-locking of the electron trajectories we build histograms of the phase difference between the trajectories considered as random variables in time, for different peak laser intensities. From the trajectories phase statistics it is seen from Fig.1 (b) that there is a characteristic jump which coincides with the dip in the ionization yield in Fig.1(c) which corresponds to the NSDI region.

Publication: I. P. Christov, “Phase-locking mechanism in non-sequential double ionization”, Appl. Phys. B 125, 1 (2019)

Spatial Non-locality in Confined Quantum Systems

In this work the TDQMC method is used to show that for parabolic core potential the range of the spatial nonlocality experienced by bosons in 1D and 2D artificial atoms (bosonic quantum dots) is limited from below by the quantum uncertainty (standard deviation of the MC sample), for both long-range and short-range interaction potentials. We study also the linear entropy as an entanglement (and correlation) measure for the bosons in the dot.

In the TDQMC method an ensemble of walkers and corresponding guide waves is attached to each physical particle such that the many-body Schrodinger equation is reduced to a number of one-body Schrodinger equations for the guide waves, which for the k-th walker from the i-th particle ensemble reads:

$$i\hbar\frac{\partial}{\partial t}\varphi_i^k(\mathbf{r}_i,t)=\left[-\frac{\hbar^2}{2m_i}\nabla_i^2+V_{e-n}(\mathbf{r}_i)+V_{eff}^k(\mathbf{r}_i,t)\right]\varphi_i^k(\mathbf{r}_i,t)$$

$i=1,\ldots,N$;
$k=1,\ldots,M$,

where $V_{e-n}(\mathbf{r}_i)$ is the classical core potential and the effective interaction potential $V_{eff}^k(\mathbf{r}_i,t)$ is given by a Monte Carlo convolution of the true potential $V_{e-e}\left[\mathbf{r}_i,\mathbf{r}_j\right]$ and the kernel function K which incorporates the specific nonlocal quantum correlation length σ_j:

$$V_{eff}^k(\mathbf{r}_i,t)=\sum_{j\neq i}^{N}\frac{1}{Z_j^k}\sum_{l}^{M}V_{e-e}\left[\mathbf{r}_i,\mathbf{r}_j^l(t)\right]K\left[\mathbf{r}_j^l(t),\mathbf{r}_j^k(t),\sigma_j\right],$$

where:

$$K\left[\mathbf{r}_j,\mathbf{r}_j^k(t),\sigma_j\right]=\exp\left(-\frac{\left|\mathbf{r}_j-\mathbf{r}_j^k(t)\right|^2}{2\sigma_j\left(\mathbf{r}_j^k,t\right)^2}\right)$$

and:

$$Z_j^k=\sum_{l=1}^{M}K\left[\mathbf{r}_j^l(t),\mathbf{r}_j^k(t),\sigma_j\right]$$

is the weighting factor.

In this way the effective potential seen by the k-th guide wave for the i-th particle involves the interaction potentials due to a number of walkers which belong to the j-th particle which lie

within the non-local length $\sigma_j\left(\mathbf{r}_j^k,t\right)$ around $\mathbf{r}_j$. The connection between the trajectories $\mathbf{r}_i^k(t)$ and the guide waves $\varphi_i^k(\mathbf{r}_i,t)$ is given by the de Broglie-Bohm guiding equations for real-time propagation:

$$\mathbf{v}_i^k(t) == \frac{\hbar}{m_i}\mathrm{Im}\left[\frac{\nabla_i\varphi_i^k(\mathbf{r}_i,t)}{\varphi_i^k(\mathbf{r}_i,t)}\right]_{\mathbf{r}_i=\mathbf{r}_i^k(t)},$$

and it is given by a drift-diffusion process for the ground-state preparation (imaginary-time propagation):

$$d\mathbf{r}_i^k(\tau) = \mathbf{v}^{Dk}{}_i d\tau + \boldsymbol{\eta}_i(\tau)\sqrt{\frac{\hbar}{m_i}d\tau},$$

where:

$$\mathbf{v}^{Dk}{}_i(\tau) = \frac{\hbar}{m_i}\left[\frac{\nabla_i\varphi_i^k(\mathbf{r}_i,\tau)}{\varphi_i^k(\mathbf{r}_i,\tau)}\right]_{\mathbf{r}_i=\mathbf{r}_i^k(\tau)}$$

is the drift velocity, and $\boldsymbol{\eta}(\tau)$ is Markovian stochastic process whose amplitude tends to zero toward steady state as $\tau^{0.2}$.

In order to explore the role of the boson-boson interaction on the spatial quantum nonlocality we calculate the ground state of 1D and 2D artificial atoms with parabolic core potential $V_{e-n}(\mathbf{r}_i) = r_i^2/2$ (bosonic quantum dots). Unlike in the standard quantum dots where there is fermionic exchange interaction which reduces the overlap between the wave functions for the equal-spin electrons here we have practically identical probability distributions for all bosons in the trap, similarly to the 1S state occupied by opposite-spin electrons in the two-electron atom. In order to explore the role of the potential range on the boson-boson correlation we have chosen Yukawa-type of soft-core repulsive potential. We have plotted in Fig.2 the energy (c) and the linear entropy (b) of 1D bosonic quantum dot with up to 6 particles, for long-range repulsive potentials, with blue and with red lines, respectively. It is seen that within the statistical error there is a good correspondence between the TDQMC results and the exact numerical results (green lines) obtained by a direct solution of the many-body Schrodinger equation for up to 4 bosons in one spatial dimension. The important result here is shown in Fig.2 (a) where one can see that the parameter $\alpha_{opt} = \sigma_j / s_j$ which minimizes the energy of the system is almost independent on the range of the interaction potential despite the larger width of the probability distribution for the short-range potential which pushes the near-range bosons further from each other thus increasing the entropy and decreasing the overall energy of the system. Also it is seen that α_{opt} increases for up to 6

bosons while it is greater than one, which means that the nonlocal length σ_j slightly exceeds the standard deviation of the MC sample in 1D.

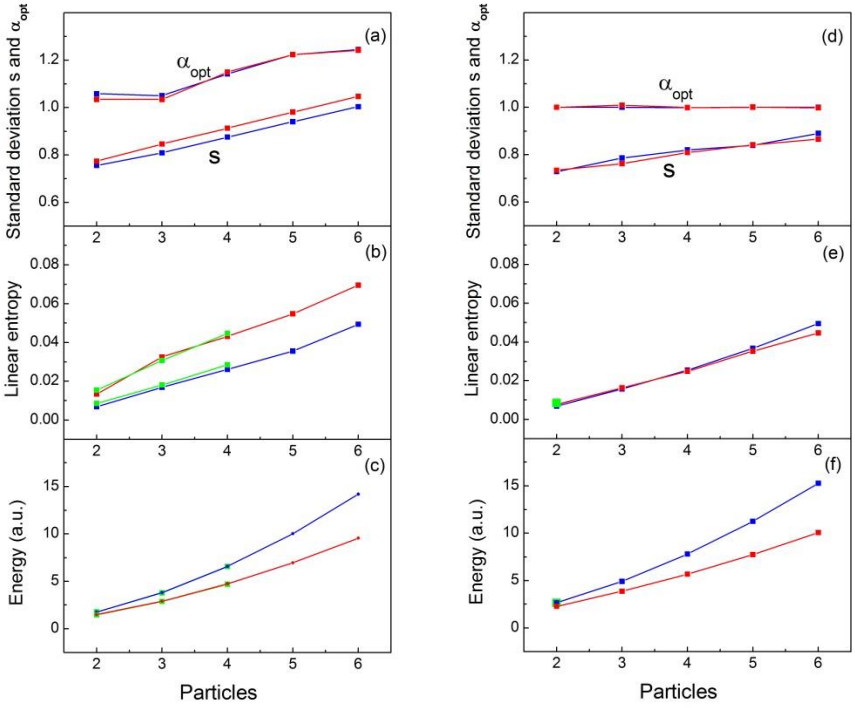

Fig.2. Spatial nonlocality parameter α_{opt} (a), (d), linear entropy (b), (e), and energy (c), (f) versus the number of bosons, for 1D quantum dot - (a) - (c) and for 2D quantum dot - (d) - (f). Blue lines for long-range potential, red lines for short-range potential, and green lines for numerically exact results.

Publication: I. P. Christov, "Spatial Non-locality in Confined Quantum Systems: A Liaison with Quantum Correlations", Few-Body Syst. 61, 45 (2020)

Spatial Entanglement of Fermions in One-Dimensional Quantum Dots

The time-dependent quantum Monte Carlo method for fermions is introduced and applied in the calculation of the entanglement of electrons in one-dimensional quantum dots with several spin-polarized and spin-compensated electron configurations. The rich statistics of wave functions provided by this method allow one to build reduced density matrices for each electron, and to quantify the spatial entanglement using measures such as quantum entropy by treating the electrons as identical or distinguishable particles. Our results indicate that the spatial entanglement in

parallel-spin configurations is rather small, and is determined mostly by the spatial quantum nonlocality introduced by the ground state. By contrast, in the spin-compensated case, the outermost opposite-spin electrons interact like bosons, which prevails their entanglement, while the inner-shell electrons remain largely at their Hartree–Fock geometry.

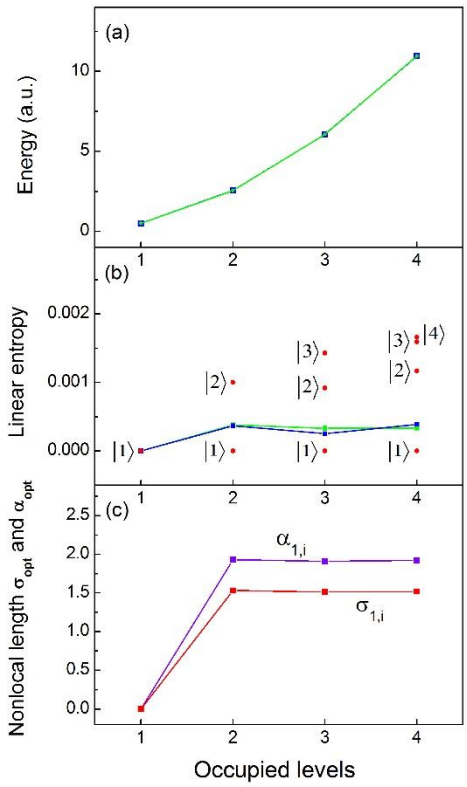

Fig. 3. Energy (**a**), linear entropy (**b**), and nonlocality parameters $\sigma_{1,i}$ ($\alpha_{1,i}$) (**c**) for the ground state $|1\rangle$, for electron configurations with up to four parallel-spin electrons (Figure 1a). Blue lines: TDQMC results; green lines: numerically exact results; red dots in (**b**): linear entropy for distinguishable electrons.

The TDQMC method transforms the standard Hartree–Fock (HF) equations into a set of coupled stochastic equations capable of describing the correlated particle motion. That transformation is based on the physical assumption that the modulus square of the single-body wave function in coordinate (physical) space may be thought of as an envelope (or kernel density estimation) of the distribution of a finite number of particles (walkers). In this way, for each electron in an atom a large set of single-body wave functions that reside in physical space-time is created, where each wave function responds to the multicore potential due to both the nucleus and the walkers of the rest of the electrons. The crucial point in this picture is that it allows for each

walker for a given electron to interact with the walkers of any other electron through weighted Coulomb potential, thus naturally incorporating the spatial quantum nonlocality. Then, from the evolution of the walker distributions one can evaluate quantum observables without resorting to the many-body wave function.

As an example here we calculate the ground state of a quantum dot with parabolic core potential $V_{en}(\mathbf{r}_i) = \omega^2 r_i^2 / 2$ and with soft-core electron–electron Coulomb repulsion:

$$V_{ee}\left[\mathbf{r}_i, \mathbf{r}_j\right] = \frac{e^2}{\sqrt{r^2 + a^2}}$$

where $r \equiv \left|\mathbf{r}_i - \mathbf{r}_j\right|$.

Figure 3a shows the calculated energies (green line), which are in a very good correspondence with the numerically exact energies (blue line) obtained from the direct numerical solution of the Schrödinger equation for up to four electrons in one spatial dimension. Our calculations reveal that accuracy of three significant digits for the energy can be attained by varying $\alpha_{1,i}$, while $\alpha_{2,i}$, $\alpha_{3,i}$, and $\alpha_{4,i}$ are set to infinity, which practically keeps the ground state at its Hartree–Fock geometry. The optimal values of $\alpha_{1,i}$ for the ground level $|1\rangle$ are shown in Figure 3c for two, three, and four electrons, also showing that both $\alpha_{1,i}$ and the nonlocal length $\sigma_{1,i}$ are almost independent of the number of electrons—except for one electron at the ground state where there is no e–e interaction—and $\alpha_{1,i}$ is set to zero. The degree of entanglement is quantified by the linear quantum entropy, as shown in Figure 3b. There are two distinct cases: In the first, the electrons are considered identical (blue line), to be compared with the result from the exact numerical solution of the Schrödinger equation (green line). It can be seen that the linear entropy in this case remains almost constant, in close agreement with the exact numerical result. The second case, plotted with red dots in Figure 3b, depicts the linear entropy for the different electrons considered as distinguishable particles with the density matrix. It can be seen that the linear entropy for the distinguishable electrons increases due to the screening effect of the inner electrons, which causes larger fluctuations in the shape of the outer wave functions.

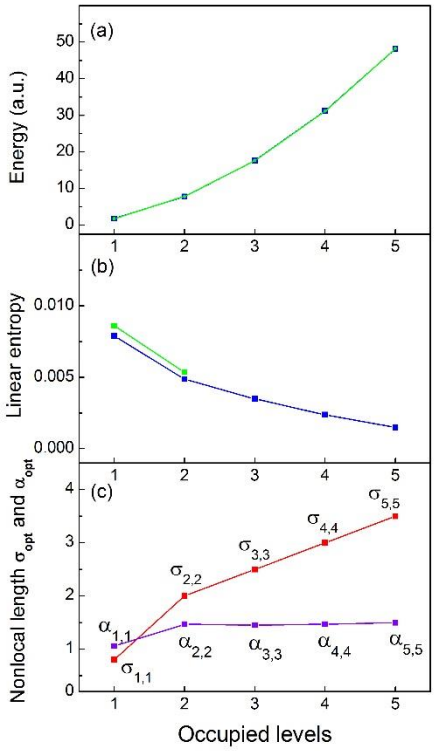

Fig. 4. Energy (**a**), linear quantum entropy (**b**), and nonlocality parameters $\sigma_{1,i}$ ($\alpha_{1,i}$) (**c**) for the outermost level $|i\rangle = |1\rangle, \ldots, |5\rangle$-, for electron configurations with up to five filled shells (Figure 1b). Blue lines: TDQMC results; green lines: numerically exact results.

In the process of adding correlated electrons at the outer shells, the inner-shell electrons remain largely intact due to their stronger localization (confinement) to the core. Therefore, to a good approximation, the inner-shell wave functions need not be recalculated, and these may remain at their self-consistent Hartree–Fock configurations. Figure 4a depicts the system energy (blue line), which almost perfectly matches the numerically exact energies (green line) obtained using the standard DMC method. The linear entropy predicted by the TDQMC method decreases when adding new excited states to the electron configuration (blue line in Figure 4b), which contrasts with the case of bosonic quantum dots, where it increases for more electrons at the ground state. This behavior is also confirmed by the numerically exact results (green line) for levels 1 and 2 (two and four identical electrons), and can be explained by the orthogonality of the wave functions in the fermionic calculation, which causes weaker interaction for the outer-shell electrons.

Publication: I. P. Christov, "Spatial Entanglement of Fermions in One-Dimensional Quantum Dots", *Entropy 23,* 868 (2021)

Conversion efficiency of high harmonic generation (HHG) in diamond

Recently HHG was observed in bulk crystals irradiated by strong mid-infrared pulses with energies of a few microjoules. Semiconductor and dielectric based HHG sources have the potential of being brighter due to the high atomic density of the bulk material. At the same time solid-state high-harmonic sources may be feasible for generation of attosecond pulses with high repetition rate. Good conversion efficiency without damage to the crystal is essential to realize the potential of solid state HHG as a high-power attosecond source.
In the reported research we investigate theoretically the time-evolution of electron excitation and high-harmonic generation in diamond bulk subjected to intense near-infrared laser pulse. We find the conversion efficiency of near-infrared to ultraviolet radiation in the material and discuss specific aspects of the subcycle structure in the transient photoelectron distribution. Publication: B. Obreshkov, T. Apostolova, Nonlinear Optics, NTu4A. 3, (OSA Technical Digest (Optical Society of America, 2019), **https://doi.org/10.1364/NLO.2019.NTu4A.3**

Ultrafast energy absorption and photoexcitation of a bulk plasmon in crystalline silicon

Time-resolved optical experiments on femtosecond laser excited dielectrics have provided evidence that ultrafast solid to liquid phase transition occurs after a large amount of laser energy is deposited in the solid material during a time interval much shorter than the time for thermalization of the absorbed energy. The photoexcitation of a critical number of electron- hole pairs results in bond softening and structural phase transition. Theoretical models have been developed aiming to investigate electronically-driven ultrafast melting mechanisms in semiconductors. These studies predict that lattice instability in the dense plasma develops once the critical density of electron-hole pairs is of an order of 10^{22} cm^{-3}. In silicon irradiated with visible wavelengths, such high densities are reached at the fluence of about 0.2 J/cm^2. Changes of optical constants of the strongly excited dielectrics are measured using pump-probe spectroscopy techniques. The high density plasma of photoexcited charge carriers leads to distinct change of the optical reflectivity. The optical reflectivity of photoexcited silicon measured as a function of the pump pulse fluence initially decreases for relatively low pump fluences and displays a sharp increase with increase of the probe pulse fluence. This was interpreted assuming that the optical properties are dominated by free-carrier response. More elaborate models for the macroscopic dielectric function of the laser-excited state incorporating Pauli blocking and screening of the Columbic electron-hole attraction were used showing good qualitative agreement with the measured dielectric function of gallium arsenide. More recently, first principle approaches based

on time-dependent density functional theory (TDDFT) have been developed and applied for understanding the optical properties and obtaining ultrafast optical breakdown thresholds of strongly excited semiconductors and dielectrics. The reflectivity of photoexcited silicon was calculated as a function of the peak laser intensity and a qualitative agreement with the experimental observation was found. Consistent interpretation of the intensity dependence of the reflectivity curve was given in terms of the simplified free electron Drude model, and more recently the dielectric response of the crystalline silicon following irradiation by a high intensity near-infrared laser pulse was obtained from numerical pump-probe experiments. The results showed that the optical response of the photo-excited silicon exhibits characteristic features of electron-hole plasma in non-equilibrium phase. The real part of the dielectric function was found to be well described by a Drude free-carrier response with screened plasma frequency determined from ground state properties. The effective mass of the charge carriers was found to increase monotonically with the increase of the laser intensity. Optical anisotropy in the response of the photoexcited solid was also reported. While standard pump-probe spectroscopy studies electronic dynamics with femtosecond time resolution, advances in laser technologies resulted in attosecond metrology. In nonlinear attosecond polarization spectroscopy, the oscillating laser electric field is used to measure the non-linear polarization which in turn determines the amount of energy reversibly or irreversibly exchanged between the electromagnetic field and the dielectric material. Nonlinear polarization spectroscopy yields more complete information about the dynamic electronic response to strong fields with attosecond time resolution, e.g, measurements utilizing attosecond spectroscopy in combination with TDDFT calculations allowed to resolve electron dynamics in crystalline silicon. Interest in the time evolution of the excitation process is motivated by applications like petahertz signal processing and mechanisms of ultrafast dielectric breakdown.

In the reported research we investigate the non-linear response and energy absorption in bulk silicon irradiated by intense 12-fs near-infrared laser pulses using the time dependent Schrödinger equation in single-active electron approximation combined self-consistently with the Maxwell's equation solved in long wavelength approximation. The empirical pseudopotential method is applied for describing the electronic properties of the material. For peak laser intensities near and above 10^{14} W/cm^2, photoionization creates dense plasma of electron-hole pairs together with a strongly absorbing state of silicon for near infrared laser wavelengths, due to excitation of bulk plasmon resonance. In this regime, the energy transfer to electrons exceeds a few times the thermal melting threshold of Si. This state may be considered as a precursor to ultrafast phase transition and melting of silicon, as reported experimentally using femtosecond lasers. Depending on the laser intensity, we distinguish two regimes of non-linear absorption of the laser energy: for low intensities, energy deposition and photoionization involve perturbative three- and four-photon transitions through the direct bandgap of silicon. Scaling laws of the absorbed energy and electron density as a function of the laser intensity are obtained. Optical constants (refractive index, extinction coefficient) and the normal incidence reflectivity of the photo excited silicon are obtained and compared to existing experimental data and other theoretical works. The optical reflectivity of the photoexcited solid is found in good qualitative agreement with existing

experimental data. In particular, the model predicts that the main features of the reflectivity curve of photoexcited Si as a function of the laser fluence are determined by the competition between state and band filling associated with the Pauli Exclusion Principle and the Drude free-carrier response. With the increase of the light pulse intensity, the number of photoexcited charged carriers increases and dense plasma of electron-hole pairs is established. When the corresponding plasma frequency matches the laser frequency, a resonant energy transfer occurs from the light pulse to the electrons and dielectric breakdown occurs associated with sharp rise of the optical reflectivity.
The non-linear response of the photoexcited solid is also investigated for irradiation of silicon with a sequence of two strong and temporary non-overlapping pulses. The cumulative effect of the two pulses is non-additive in terms of deposited energy. Photoionization and energy absorption on the leading edge of the second pulse is greatly enhanced due to free carrier absorption.

Publications: T.Apostolova, B.Obreshkov and I. Gnilitskyi, arXiv preprint arXiv:1910.09023 , 2019, T. Apostolova, B. Obreshkov and I. Gnilitskyi, Applied Surface Science 519 (2020) 146087

Femtosecond optical breakdown of silicon

Using the same numerical method we also investigate photoinization, energy deposition, plasma formation and the ultrafast optical breakdown in crystalline silicon irradiated by intense near-infrared laser pulses with pulse duration < 100 fs. The occurrence of high-intensity breakdown was established by the sudden increase of the absorbed laser energy inside the bulk, which corresponds to threshold energy fluence 1 J/cm^2. The optical breakdown is accompanied by severe spectral broadening of the transmitted pulse. For the studied irradiation conditions, we find that the threshold fluence increases linearly with the increase of the pulse duration, while the corresponding laser intensity threshold decreases. The effect of the high plasma density on the stability of diamond lattice is also examined. For near threshold fluences, when about 5 % of valence electrons are promoted into the conduction band, the Si-Si bonds are softened and large Fermi degeneracy pressure arises (with pressure up to 100 kbar). The mechanical instability of the diamond lattice suggests that the large number of electron-hole pairs leads directly to ultrafast melting of the crystal structure.

Publications: T.Apostolova and B.Obreshkov submitted_to_Applied Surface Science (2021), preprint at arXiv:2107.07189 **[**cond-mat.mtrl-sci**]**

High Harmonic generation in silicon

We study the generation of high order harmonics in crystalline silicon subjected to intense near-infrared 30fs laser pulses. The harmonic spectrum extends from the near infrared to the extreme ultraviolet spectral region. Depending on the pulsed laser intensity, we distinguish two regimes of harmonic generation: (i) perturbative regime: electron-hole pairs born during each half-cycle of the laser pulse via multiphoton and tunnel transitions are accelerated in the laser electric field and gain kinetic energy; the electron-hole pairs then recombine in the ground state by emitting a single high-energy photon. The resultant high harmonic spectrum consists of sharp peaks at odd harmonic orders. (ii) non-perturbative regime: the intensity of the harmonics increases, their spectral width broadens and the position of harmonics shifts to shorter wavelengths. The blueshifts of high harmonics in silicon are independent on the harmonic order which may be helpful in the design of continuously tunable XUV sources.

Publications: B.Obreshkov and T.Apostolova Journal of Physics: Conference Series **1571** (2020) 012012, doi:10.1088/1742-6596/1571/1/012012

We also investigate the high harmonic generation in bulk silicon irradiated by intense near-infrared laser pulses with varying pulse duration < 100$ fs. Depending on the laser intensity we distinguish two regimes: Perturbative regime - electron-hole pairs born during each half-cycle of the laser pulse via multiphoton and tunnel transitions are accelerated in the laser electric field and gain kinetic energy; subsequently the photoexcited pairs recombine by emitting a single high-energy photon. Harmonics are emitted with alternating phase during half-cycle of the driving laser pulse. The resultant high harmonic spectrum consists of isolated peaks at odd harmonic orders. Emission of even order harmonics is also observed with the increase of the pulse duration due to optical rectification of the transmitted pulse. The breakdown regime is characterized by the formation of dense plasma of electron-hole pairs and severe spectral broadening of the transmitted pulse. The resultant harmonic spectrum superimposes onto a continuous background, the spectral width of individual harmonics is substantially broadened and their central wavelength undergoes a blue shift that covers the spacing between adjacent harmonic orders.

Publications: T.Apostolova and B.Obreshkov submitted to EPJD (2021)